A technique for medium-range through-thickness focusing using Lamb waves

Konstantinos Tzaferis*, Gordon Dobie, Dave Lines, Charles MacLeod
Centre for Ultrasonic Engineering, Department of Electronic and Electrical Engineering, University of Strathclyde, Glasgow, G11XW, UK
* Corresponding author, e-mail: konstantinos.tzaferis@strath.ac.uk

Abstract

Medium-range guided wave testing is commonly employed for inspection of areas with restricted access. The technique usually works in pulse echo mode and at high frequency-thickness products, around 20 MHz·mm, offering good sensitivity and resolution. Defect sizing is based on the reflection amplitude of the received mode(s). However, the scattering of guided waves is complex, and the amplitude of the reflected modes does not provide sufficient information for defect sizing. This work aims to overcome this limitation using a focusing technique based on Lamb waves. Specifically, multiple Lamb wave modes are excited individually and superimposed to form a new mode with a desired through-thickness energy distribution. This way, energy is focused on a single point in the structure. Using weighting functions, the location of the focal point is swept across the thickness of the sample. The technique allows for accurate sizing of flaws, such as cracks and wall loss.

Keywords: Lamb wave focusing, Medium-range guided waves, High-resolution guided waves

1. Introduction

Ultrasonic guided waves are commonly used for the non-destructive testing of plates and pipes. They can be employed to quantify wall loss [1–4], axial and/or circumferential cracks [5,6] and other flaws. The choice of guided wave inspection method depends on the specific inspection requirements, such as sensitivity, resolution, and inspection range.

Long-range guided wave testing is commonly employed for the inspection of pipework, such as pipe racks and transmission lines [7,8]. Large lengths (typically around 100 m) are screened with a single capture, making the technique time-efficient and practical. Potential problem areas are identified and are further investigated using a more precise method to determine the exact dimensions of the defect.

Compared to long-range, medium-range guided wave testing offers higher sensitivity and resolution but a shorter inspection range [9–11]. Ultimately, the technique is an intermediate step between bulk wave and long-range guided wave testing. The approach is attractive in cases where high accuracy is needed, however direct access to the test component is limited or time is sensitive. Relevant applications include but are not limited to the inspection of the annular plate of above ground storage tanks, inspection for corrosion under pipe supports, and in-process weld inspection of thin plates at the point of manufacture [12–14].

Although a fair body of work is committed to the development of medium-range guided wave testing, there are still important considerations that limit the wide application of the technique. Specifically, while it has been shown that a single guided wave mode can be generated and received [10,15,16], it is difficult to size indications reliably and determine the severity of damage using purely the amplitude of the reflection of the received modes. The scattering behavior of ultrasonic waves is complex and depends on defect size, orientation, and geometry. Moreover, the variation in energy distribution across modes means there is no consistency in the reflectivity from different flaws.

In this work, a technique is presented to perform focusing on medium-range distances using guided wave modes. Specifically, multiple higher modes are selectively excited and time delayed to arrive simultaneously at a selected cross section, say x_{cs}, as shown in Figure 1. The modes are then weighted and superimposed so that energy is focused at a specific point at (x_{cs}, z_f). By altering the modal weights, the focal point can be swept across the thickness of the plate.

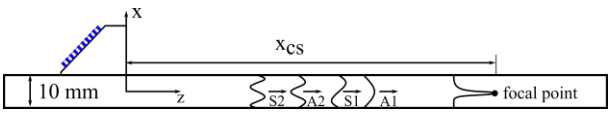

Figure 1. Schematic showing Lamb wave focusing approach. Multiple guided wave modes are combined to focus the energy at a specific cross section x_{cs} and depth.

The structure of this paper is as follows. First, in Section 2, Lamb wave focusing is presented, and analytical results are outlined. Next, in Section 3, simulation results are presented, testing the technique against various defects. Then, in Section 4, experimental results are illustrated and discussed. Finally, in Section 5, key conclusions are drawn.

2. Theory

In this section, the fundamental theory for Lamb wave focusing is outlined. The excitation of Lamb waves at high frequency-thickness products is discussed in Section 2.1. In Section 2.2, the details of the method are presented. A sensitivity analysis is performed in Section 2.3, to study how various parameters affect focusing.

2.1 Single mode excitation at high frequency-thickness products

At high frequency-thickness products, around 20 MHz·mm, the first few higher order modes exhibit little dispersion and have small wavelengths. These properties make them attractive for medium-range non-destructive testing applications.

Figure 2 displays the through-thickness compressional σ_{11} and shear σ_{13} stress components of the first four higher order modes for a 10 mm thick plate. Mode A1 has a dominant shear stress component, as shown in Figure 2 (a). Energy is concentrated at the middle of the plate. Figure 2 (b) illustrates the stress profiles of mode S2. The shear wave stress is still dominant, maximizing at ¼ and ¾ of the plate thickness. Modes A2 and S2 have both stress fields dominant, as shown in Figure 2 (c) and (d), respectively. These four modes are individually excited and superimposed to form a new desired energy distribution. Since all modes have a dominant shear stress profile, this is selected for Lamb wave focusing. To simplify the notation, in what follows, $\sigma \coloneqq \sigma_{13}$.

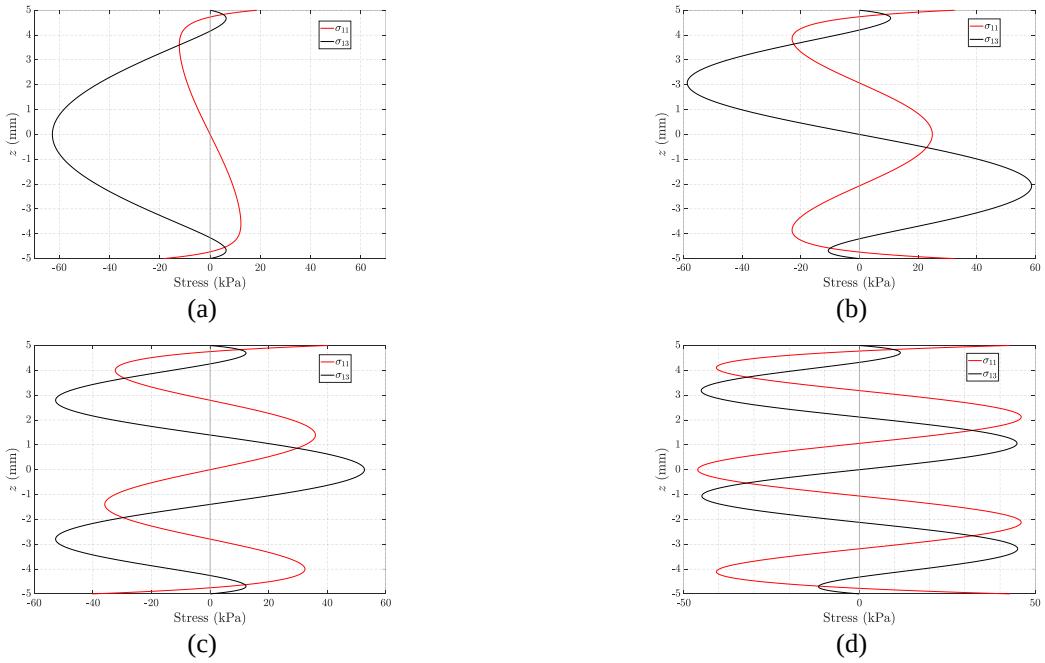

Figure 2. Stress profiles along the thickness direction of mode: (a) A1, (b) S1, (c) A2 and (d) S2.

Consider an N element array probe with pitch s mounted on a wedge of angle θ_w, as shown schematically in Figure 3. The aperture length of the array is $D \approx Ns$. Applying a linear time delay law, ultrasonic waves are steered at an angle θ_s with respect to the wedge angle. Therefore, by varying θ_s, the angle of incidence, given by

$$\theta = \theta_w + \theta_s$$

can be selected to dynamically target more than one guided wave mode. The plot of frequency versus coincidence angle is shown in Figure 4. The first four higher order modes are densely packed around 20 MHz·mm. Unless care is taken, multiple modes are generated simultaneously and propagate in the sample.

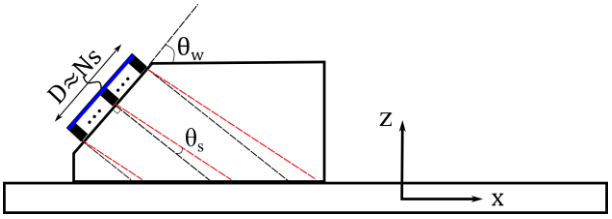

Figure 3. Schematic of an array probe mounted on an angled wedge.

The generation of a guided wave mode is primarily determined by the excitation spectrum H [17]. The excitation spectrum is proportional to the amplitude of a mode, $A \propto H$. Therefore, to enhance a mode, say at (ω_e, k_e), it must be true that

$$\frac{H(\omega_e, k_e)}{H(\omega_s, k_s)} \gg 1,$$

where (ω_s, k_s) corresponds to any mode that needs to be suppressed. The excitation spectrum of a single element probe mounted on an angled wedge is given by Rose [17]. In the case of an array probe, the spectrum appears in the more general form,

$$H(c_p, \omega; N, s, \theta_w, \theta_s) = 2\frac{\sin\left(0.5Nscos\theta_s((\omega/c_w)\tan\theta - \omega/c_p cos\theta\right)}{\left(\frac{\omega}{c_w}\right)\sin\theta - \frac{\omega}{c_p}} \quad (1)$$

If no time delays are applied, $\theta_s = 0$, and the spectrum is identical to the single-element transducer case. The plot of equation (1) in the frequency-phase velocity domain is shown in Figure 5. At high frequencies, the spectrum appears as a horizontal line and has a phase velocity bandwidth. The phase velocity bandwidth of H at -9 dB reads

$$\Delta c_p(N, s, \theta_s, \theta_w) = \frac{\frac{K}{\pi}\frac{\lambda_e}{D'}}{1 - \left(\frac{K}{2\pi}\right)^2\left(\frac{\lambda_e}{D'}\right)^2}$$

where $\lambda_e = c_{pe}/f$, $D' = Nscos\theta_s/cos\theta$ and $K = 4.398$ [17]. For a 32-element array with a 1 mm pitch and targeting mode $A1$ at 1.9 MHz, $\lambda_e = 1.7$ mm and thus $\Delta c_p = 0.051$ mm/s. The phase velocity separation between modes A1 and S1 can be found from the dispersion curves to be $\Delta c_p^{S1-A1} = 3.296 - 3.243 = 0.053$ mm/s. Thus, since $\Delta c_p/2 < \Delta c_p^{A1-S1}$, mode A1 can be targeted and solely excited. Since the rest of the higher order modes are more separated, it follows that these modes can be excited individually.

Besides the excitation spectrum, excitation of a single mode in a high frequency-thickness product region, around 20 MHz·mm, requires a narrow frequency bandwidth. In practice, this requires a temporal excitation with a relatively large number of cycles. The effect of the frequency bandwidth on the excitation of a single mode is studied experimentally and presented later in Section 4.1.

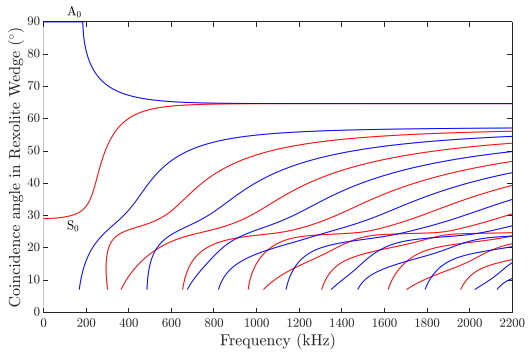

Figure 4. Frequency vs. coincidence angle of Rexolite® wedge on a 10 mm thick aluminum plate.

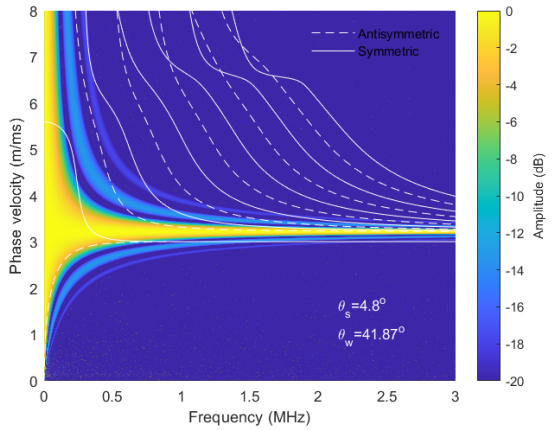

Figure 5. Excitation spectrum of an array mounted on an angle wedge in the frequency-phase velocity domain.

2.2 Through-thickness multi-modal focusing

To focus the acoustic energy at a specific point along the thickness direction, multiple modes are utilized. Each mode has a different shear stress distribution, denoted $\sigma^m(z)$. The modes can be superimposed to create a new modal profile,

$$\overline{\sigma}(z) = \sum_{m=1}^{M} w_m \sigma^m(z) \tag{2}$$

where M is the number of modes used and w_m is a weight associated with mode m. Obviously, different weight values generate different stress profiles. Therefore, the weights need to be appropriately selected to match a desired profile, say

$$\hat{\sigma}(z; z_f, \sigma) = e^{-\frac{(z-z_f)^2}{2\sigma_f^2}} \tag{3}$$

where z_f is the focal point and σ_f is the width of the focal point at -3.3dB. Indeed, it is straightforward to determine the weights after discretization along the z-axis and using the Gram-Schmidt process. Figure 6 shows the absolute value of the desired and obtained stress profiles after implementation of the Gram-Schmidt algorithm using the first six higher order modes, namely A1, S1, …, S3. The focal point width was set to $\sigma_f =$ 1mm. Smaller focal widths yield poorer focusing profiles, thus the $\sigma_f = 1$ mm was used. The results indicate energy is successfully concentrated for z_f 0, -2 and -3 mm. However, when focusing closer to the bottom surface of the plate, namely at $z_f = -4$ mm, the agreement between the obtained and the desired profiles is poor. Therefore, the technique has a 'dead zone' close to the bottom surface. The depth of the dead zone is approximately 1.5 mm. Since the focusing results are symmetric along the z axis, an identical dead zone appears close to the top surface. Although the Rayleigh wave can be potentially used for inspection of the top surface of the plate, it cannot be used with a conventional wedge as it is damped by the wedge [15].

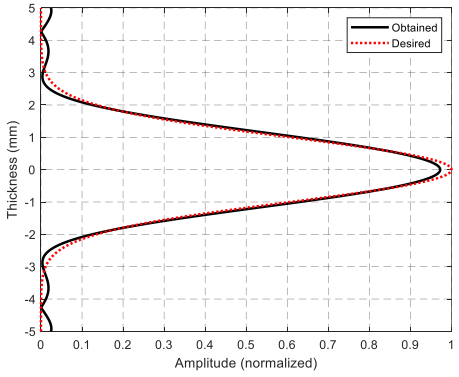

(a)

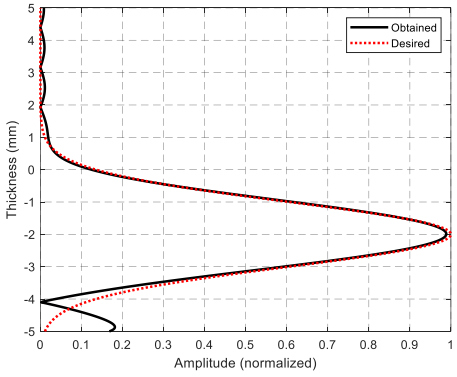

(b)

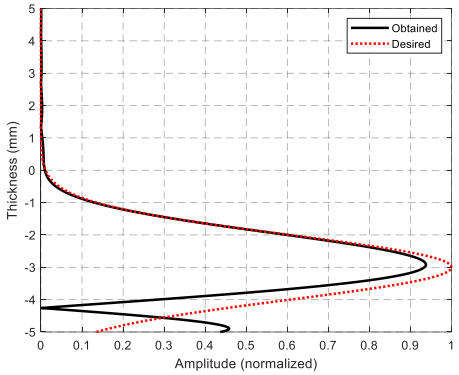

(c)

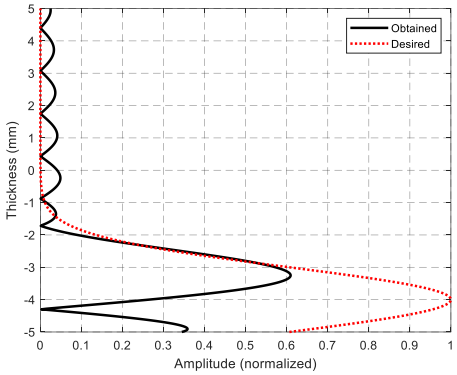

(d)

Figure 6. Desired vs. Obtained focusing profiles for $\sigma_f = 1$ mm and: (a) $z_f = 0$ mm, (b) $z_f = -2$ mm, (c) $z_f = -3$ mm, (d) $z_f = -4$ mm.

To decide the performance of different modal combinations on focusing, a similarity metric is derived, given by

$$s(z_f;\sigma_f) = \frac{\int_{-h}^{h}\int_{-h}^{-h}\overline{\sigma}(z,z_f)\hat{\sigma}(z,z_f)dzdz_f}{\int_{-h}^{h}\int_{-h}^{-h}\overline{\sigma}(z,z_f)\hat{\sigma}(z,z_f)dzdz_f}.$$

Assuming a perfect match between the desired and obtained profiles at all focal points z_f, the similarity metric equals to one. The metric varies between 0 and 1, giving a score for each combination of modes. The result of the similarity metric for combinations of different modes is shown in Figure 7. The result indicates low focusing resolution when using only two modes, A1 and S1. When four modes are considered, namely A1, S1, A2 and S2, the focusing resolution is significantly improved. Superimposing six modes slightly improves the result. Using eight modes barely improves the result. Since adding more modes makes the experimental analysis more involved, practically adding more than six modes does not improve focusing.

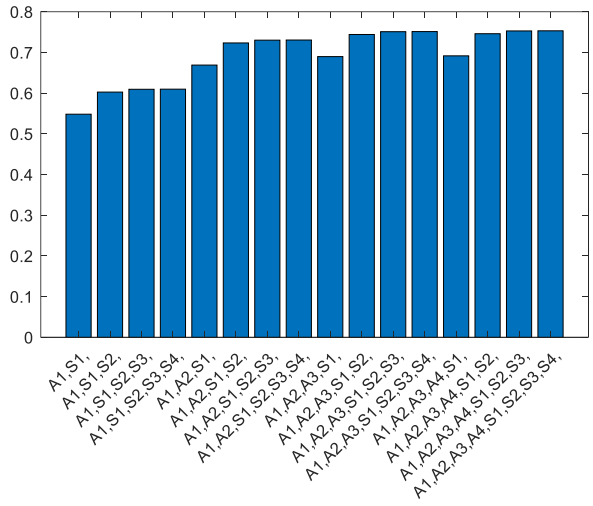

Figure 7. Similarity metric value for different modal combinations.

Next, the distribution of stress along the x-axis is investigated. Consider the time-harmonic case of equation (2),

$$\overline{\sigma}(x,z,t;z_f,\sigma_f) = \sum_{m=1}^{\mathrm{M}} \sigma^m(z) w_m(z_f,\sigma_f) e^{i(\mathrm{k}^m x-\omega t+\psi^m)}. \tag{4}$$

Assuming that the total phase is zero at (t_{cs}, x_{cs}),

$$\phi^m = k^m x_{cs} - \omega t_{cs} + \psi^m = 0, \tag{5}$$

the phase at a distance b away from x_{cs} reads

$$\phi^m = k^m(x_{cs} + b) - \omega t_{cs} + \psi^m = 2\pi \frac{b}{\lambda^m}. \quad (6)$$

Equation (6) shows that for $b \neq 0$, phase angles contribute to the sum of (4). Figure 8 shows the energy distribution along the x-z plane for focusing at four different depths, namely $z_f = 0, -1, -2$ and -3 mm. Modes A1, S1, A2 and S2 were utilized using equation (4). Note that although the waves are time harmonic and extend infinitely along the x-axis, the energy drops further away from x_{cs}. The reason is that each mode has a different wavelength; thus at distances far from x_{cs}, the modes are not in phase and can cancel each other. In practice, the excitation signal is not time-harmonic and has a non-zero frequency bandwidth. Therefore, the axial length of the wave packet is limited due to the finite duration of the excitation toneburst.

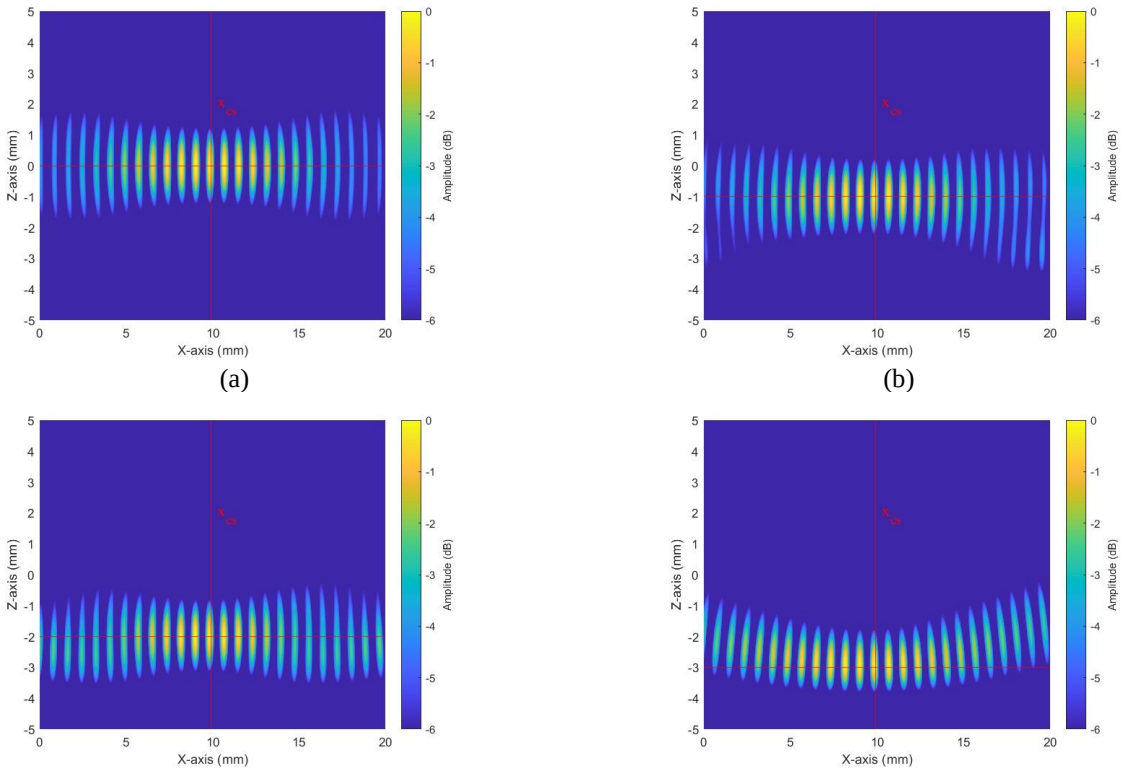

Figure 8. Energy distribution at x-z plane after superposition of time-harmonic guided waves at $x = x_{cs} =$ 10 mm and $t = t_{cr} = 4.34\ \mu s$, using the first 4 modes.

2.3 Sensitivity

2.3.1 Sensitivity to phase

So far, it is assumed that all modes are in phase at a desired cross-section, say x_{cs}. In practice, this can be achieved by time shifting the modes to arrive simultaneously at the same cross section. This is performed in simulation and experiments sections as a preliminary step. However, the process of determining the time delays is error prone, which leads to errors in focusing. Consider again the time-harmonic case using modes A1, S1, A2 and S2. The focusing profile is given by equation (4). The phase angle ψ^m can be expressed as

$$\psi^m = \psi_0^m + \psi_1^m,$$

where ψ_0^m is an arbitrary phase angle and ψ_1^m is a phase shift. The phase shift is selected so that all modes arrive simultaneously at $x = x_{cs}$,

$$\phi^m = 0 \rightarrow \psi_1^m = -k^m x_{cs} + \omega t_{cs} - \psi_0^m.$$

However, small errors in phase shifts might occur, thus

$$\psi_1^m = \psi_1^m + \psi_{er}^m,$$

and

$$\phi^m = k^m x_{cs} - \omega t_{cs} + \psi_0^m + \psi_1^m + \psi_{er}^m = \psi_{er}^m.$$

If the phase error ψ_{er}^m reaches 90°, the contribution of the mode m to the focused profile becomes zero. Moreover, in the case where $\psi_{er}^m = 180°$, the inverted profile contributes to the sum of equation (4). This is

equivalent to multiplying the mode with a negative weight value and has undesirable results.

Figure 9 displays the sensitivity of the similarity metric to phase changes of a given mode. Each curve is obtained by increasing the phase error of only the corresponding mode, whereas all other modes are assumed to be in phase. For example, the curve corresponding to mode A1 (in blue) is obtained by keeping $\psi_{err}^{m} = 0, m = 2,3,4$ and varying ψ_{err}^{1} from 0° to 360°. When the phase error is zero, all modes are in phase and the similarity metric is about 0.7. As phase changes are introduced, the similarity metric decreases, reaching its minimum value at 180°, when the modes are out of phase. As the phase error further increases, the similarity metric also increases, until it reaches its maximum value at 360°. All modes show the same pattern; however the similarity metric is most sensitive to phase changes of mode A1. This implies mode A1 has a significant contribution to equation (4). As modal order increases, the similarity metric is less sensitive to phase errors. The similarity metric is above 0.65 when the phase error is below 35°. At 2 MHz, the corresponding time delay error is $t_{error} = \frac{0.6109}{2\pi f} = 48.6$ ns.

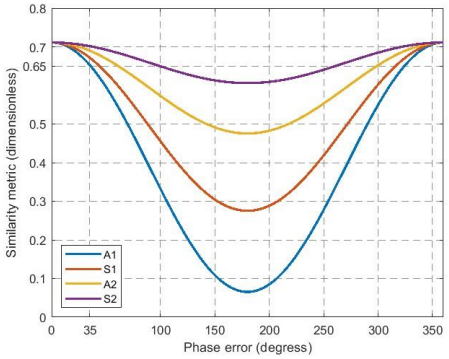

Figure 9. Sensitivity with respect to phase error of modes A1, S1, A2 and S2.

2.3.2 Sensitivity to small thickness variations

Consider a plate-like structure with a nominal thickness of 10 mm and a small smooth local thickness variation, as shown in Figure 10. The wall thickness of a 10 mm thick plate reads

$$d(x) = 10 - \Psi(x),$$

where the indentation function Ψ can be put in the following form

$$\Psi(x) = \begin{cases} \frac{\alpha}{e^{-1}} e^{\frac{-1}{1-\left(\frac{x}{\beta}\right)^2}}, x \in (-\beta, \quad \beta), \\ 0, otherwise \end{cases}$$

where α is the height and 2β is the length of the indentation.

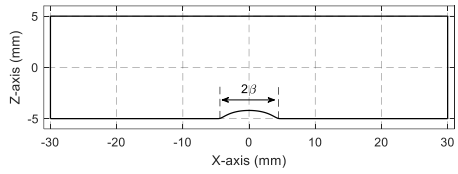

Figure 10. Plate with an indentation of 1 mm extending for 10 mm.

As guided waves propagate through the indentation region, their operating frequency-thickness product slightly changes. Therefore, the propagation speed also changes, and this can lead to phase errors. Assuming time-harmonic waves, the travel time through the wall loss is

$$t_{bump} = \int_0^{2\beta} \frac{1}{c_p(d(x))}\, dx\,,$$

where the time required to travel a distance of l when the plate is intact is simply

$$t_{int} = \frac{2\beta}{c_p}.$$

Therefore, the phase difference between the two cases can be written in the following form,

$$\phi_{shift} = \omega\left(t_{int} - t_{bump}\right). \tag{7}$$

The plot of equation (7) with respect to indentation length is shown in Figure 11 (a). As expected, in the absence of the indentation, the phase difference is zero. As the indentation length increases, the difference in phase increases linearly. Mode $A1$ exhibits the smallest slope as is the least dispersive amongst the four modes. This is beneficial, as focusing is mostly sensitive to phase changes in mode A1 (see Figure 9.) The plot of indentation length vs. the similarity metric is given in Figure 11 (b). For lengths smaller than 15 mm, the similarity metric is above 0.65. This means that small thickness variations with a length less than or equal to approximately $9\lambda_{A1}$ (15 mm), do not significantly affect the technique.

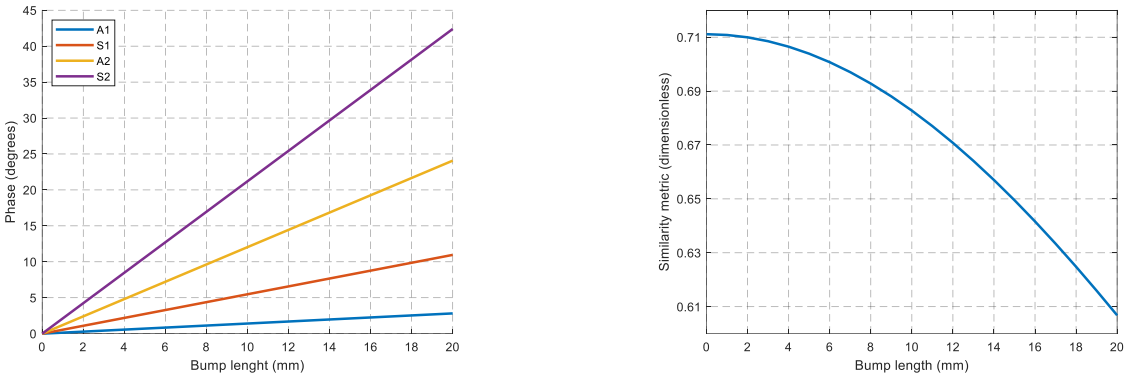

(a) (b)

Figure 11. Indentation length vs.: (a) phase change of each mode, (b) similarity metric.

3. Simulations

To capture the fundamental physics and speed up simulation time, 2D finite element simulations [18] were developed using OnScale [19]. The mesh size was set to 0.05 mm, which resulted in more than 20 nodes per wavelength [20]. The timestep was set to 5 ns, which is lower than the time required for the fastest wave to travel through an element of the given size [21].

In Section 3.1, a preliminary set of simulations was performed on an intact plate. In Section 3.2, focusing simulations were performed on a series of different notches to evaluate the sensitivity and resolution of the technique. Focusing was performed using the first four higher order modes, namely A1, S1, A2 and S2.

Table 1. Simulation parameters

Parameters	Wedge Velocity	Wedge Angle	Plate thickness	Plate long. Velocity	Plate shear velocity	Plate density	Array elements	Array pitch	Array element width	Excitation signal center frequency	Excitation signal number of cycles
	2343 m/s	41.69°	10 mm	6473 m/s	3226 m/s	2700 kg/m^3	32	1 mm	0.75 mm	1.9 MHz	5-A1 15-S1,A2,S2

3.1 Extraction of time of arrival and stress profiles on an intact plate

A schematic of the simulation set-up is shown in Figure 12. An angled wedge is located on top of a 10 mm thick plate. A 32-element array is mounted on top of the wedge. The array emits plane waves by applying a piston-like pressure load at the wedge-element interface. Using beam steering, guided wave modes are excited. Each mode is excited individually, thus requires a separate simulation. The simulation parameters are given in Table 1.

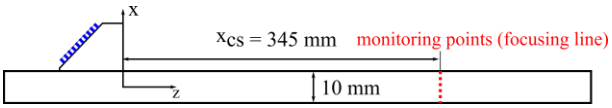

Figure 12. Schematic of simulation set-up.

Four simulations were performed to determine the time of arrival t^m and stress profile σ^m of each mode across the cross section at x_{cs}. The time of arrival is defined here as the time when the stress σ^m maximizes. Extracting the time of arrival allows time shifting the modes to arrive simultaneously at x_{cs}. Modes A1, S1, A2 and S2 were generated and received using a vertical monitoring line located at x_{cs}. To keep the results general, x_{cs} was arbitrary selected 345 mm away from the front face of the wedge. The time of arrival of each mode is shown in Table 2. The stress profile σ^m along the z-direction was also recorded. This profile is essentially identical to that of Figure 2, so it is not repeated here.

Table 2. Time of arrival at cross section 345 mm away from the wedge

Mode	A1	S1	A2	S2
Time of arrival (μs)	132.6	138.0	142.0	147.5

3.2 Lamb wave focusing

Next, Lamb wave focusing is evaluated against different notches. The length, depth, and position of the notch are varied to evaluate the sensitivity of the technique to different types of flaws. Short and deep notches are simple models of a crack or sharp pit, whereas larger and shallower notches may be used to model a corrosion patch. Unless otherwise stated, all parameters in the simulations are identical to the ones used in Section 3.1.

3.2.2 Focusing at a notch

The simulation set-up is shown in Figure 13. A notch of length ℓ_{notch} and depth d_{notch} is modeled. The notch is located 345 mm away from the front face of the wedge, as in Section 3.1. Modes A1, S1, A2 and S2 are excited separately and received independently by all array elements, thus operating in pulse echo mode.

Focusing is performed in post-processing at the front (insonified) face of the notch. The focal points lie at (x_{cs}, z_f) and their number depends on the step of discretization, which was selected 0.25 mm. First, the received signals are phased according to Table 2. Then, for each focal point, guided wave modes are weighted and summed, according to equation (2). This leads to the construction of a matrix of the form $[z_f \times R_x \times t]$. Then, for each focal point (x_{cs}, z_f), the signals are beamformed and the reflection amplitude $R(z_f)$ is calculated. It is expected that $R(z_f)$ is large when a reflector is present and small in the absence of a reflector. The beamforming is semi-synthetic, as Lamb waves are physically propagating, but they are superimposed and focused synthetically.

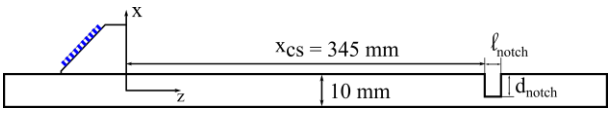

Figure 13. Schematic of simulation set-up to image a vertical notch.

3.2.2.1 Effect of notch length

Three different notches with varying lengths were simulated. The lengths of the notches were chosen to be $\frac{\ell_{notch}=\lambda_{A1}}{4}$, λ_{A1} and $5\lambda_{A1}$, where λ_{A1} is the wavelength of mode A1 and equals 1.7 mm. The depth of the notches was kept constant at 50% thickness. The beamforming, by combination of the different modes, is as per the methodology outlined in equation (3) and this is used to step the focus throughout the thickness. Specifically, the focal point z_f was swept from -3.5 to 3.5 mm with a step of 0.25 mm and the focal width was set to $\sigma_f = 1$ mm. For $z > 3.5$ and $z < -3.5$, i.e. close to the top and bottom surfaces of the plate, the

technique has no focusing ability (see Figure 6). Figure 14 illustrates the reflection amplitude $R_{notch}(z_f)$ against z_f. The 0 dB value is common for all three cases. Little change is observed between the three cases, meaning the technique is insensitive to length variations, even for lengths smaller than the wavelength. The 0 dB value is common for all three cases. Moreover, the depth of the notch can be accurately estimated. Specifically, a strong reflection is obtained when focusing along the face of the notch. The reflection amplitude is around 0 dB, with a variation of around 1.5 dB. When focusing on depths below the notch, the reflection amplitude drops by 8 dB, with a variation of around 1.5 dB. The depth of the notch can be estimated at

$$R_{call} = \frac{\max R_{notch} + \min R_{notch}}{2} \tag{8}$$

where $maxR_{notch}$ and $minR_{notch}$ are the maximum and minimum of the reflection amplitude, respectively. The call line is shown as a horizontal line at $z = -0.15$ mm. The estimated depth is thus 51.5%.

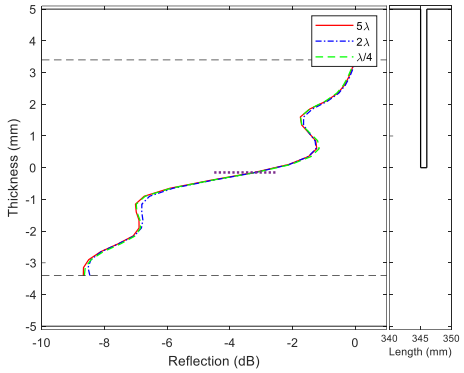

Figure 14. Focusing reflection of a 50% deep notch of length $5\lambda_{A1}, 2\lambda_{A1}$ and $\lambda_{A1}/4$.

3.2.2.2 Effect of notch depth

The effect of notch depth is studied. Three top surface notches were simulated at corresponding depths of 35%, 50% and 70%. The length was kept equal to λ_{A1}. Figure 15 illustrates the reflection amplitude for each case. The reflection from the 35% deep notch is shown in red. As expected, the reflection amplitude is approximately constant when focusing along the face of the defect; however it drops significantly when focusing below the notch. The same pattern is observed for the 50% and 70% notches, shown in blue and green, respectively. These results indicate the depth of the notch can be accurately obtained using equation (8). Moreover, three bottom surface notches were simulated. The reflection amplitude vs. focal point is shown in Figure 16. Again, the reflection amplitude drops when focusing away from the defect face. Nevertheless, the reflection locally peaks at some unwanted locations, for example, around $z = 1.5$ mm for the 50% deep notch. This could be due to the size of the focal point, which is around 1 mm, but in any case, the increase in reflection amplitude is small and local.

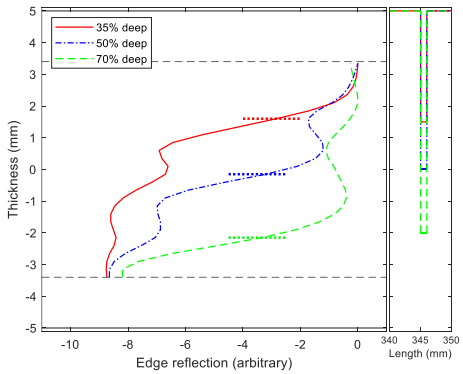

Figure 15. Focusing reflection varying the depth of a top surface notch.

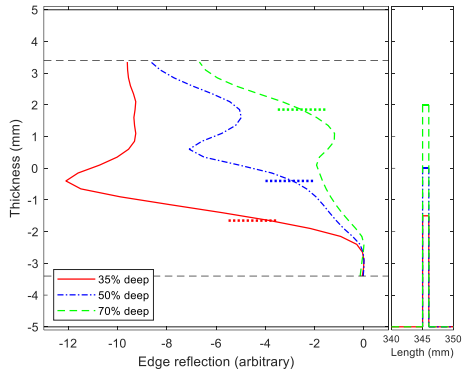

Figure 16. Focusing reflection varying the depth of a bottom surface notch.

3.2.3 Focusing at internal notches

To further test the technique, focusing was performed at internal crack-like notches. Four notches were simulated, with a vertical length of $\sigma_f/2, \sigma_f, 2\sigma_f$ and $4\sigma_f$. The center of all notches was at $z = 0$ mm. The reflection amplitude along the thickness direction is shown in Figure 17. Although in all cases the highest reflection is obtained at the crack face, accurate estimation of the crack's vertical length using equation (8) is possible for crack lengths larger than the focal width. Specifically, cracks with vertical length equal to $2\sigma_f, 4\sigma_f$ were overestimated with an error of 13% and 15%, respectively, whereas cracks with vertical length equal to $\sigma_f/2, \sigma_f$ were overestimated with 81% and 54% error. The reflection amplitude for the first three notches is very similar.

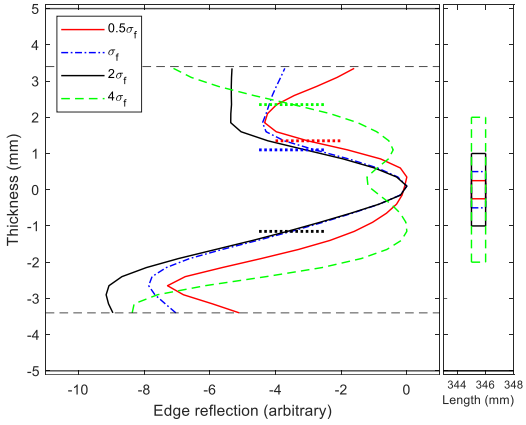

Figure 17. Focusing on a crack-like notch of depth $\frac{\sigma_f}{2}, \sigma_f, 2\sigma_f$ and $4\sigma_f$.

4. Experimental results

4.1 Influence of steering angle and frequency bandwidth

4.1.1 Effect of steering angle

The SANR (signal-to-ambient-noise ratio) angle is defined as the angle that maximizes the energy dissipated in the targeted mode, i.e., maximizes the SANR. The SANR angle is determined experimentally and should coincide with the theoretical steering angle. The steering angle vs. signal amplitude for the first six higher order modes is shown in Figure 18. To extract the amplitude, at each angle, the Hilbert envelope of the signal is obtained, and the maximum of the Hilbert envelope is plotted. For each mode, the amplitude peaks at the SANR angle. As expected, as the modal order increases, the SANR angles are further separated from each other.

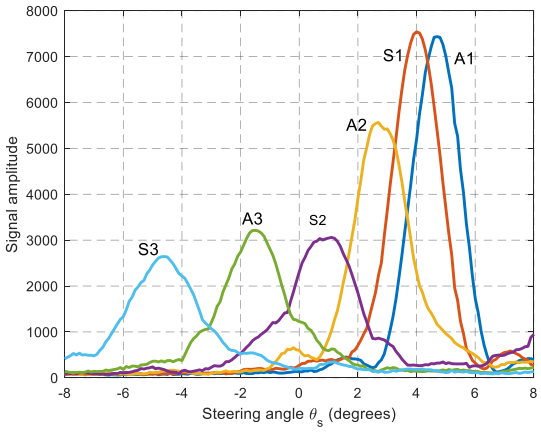

Figure 18. Steering angle vs. signal amplitude. The SANR angle is where amplitude peaks.

For single-mode excitation, it is usually beneficial to select an excitation angle slightly different from the SANR angle. The SMNR (signal-to-modal-noise ratio) angle is defined as the angle that maximizes the SMNR,

$$R_{opt} = \frac{M_e}{M_s} \quad ,$$

where M_e is a mode to enhance and M_s are the selected modes to suppress, which are usually the neighboring modes of M_e. The SMNR angle is not necessarily equal to the SANR angle. However, both angles must have similar values, because if not, the SANR drops significantly and the excitation is suboptimal. For this reason, the SMNR angle is not allowed to cause an amplitude drop of less than -2.5 dB.

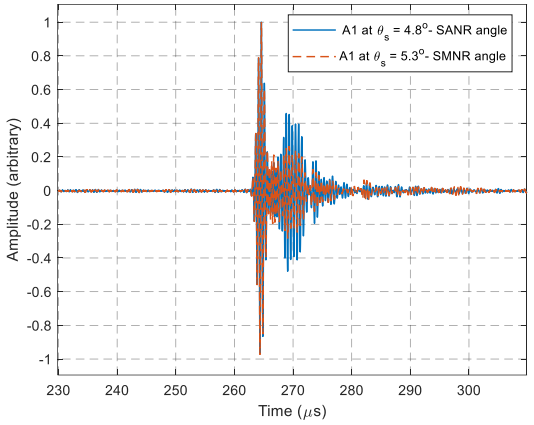

Figure 19. A-scan comparing the ratio between mode A1 (targeted) and S1 (unwanted) for different steering angles.

Consider for example mode A1. In contrast to other modes, mode A1 has a single neighbor in the dispersion diagram, namely mode S1 (neglecting the Rayleigh wave). It can be shown that the amplitude ratio A1/S1 is monotonically increasing as the angle of incidence exceeds the SANR angle. However, the overall energy dissipated to mode A1 decreases, and there is a trade-off between single-mode excitation and energy dissipation. A good compromise was found at 5.3 degrees, where the amplitude drop of mode A1 is -2.5 dB and the A1/S1 ratio is significantly improved, as shown in Figure 19. A similar analysis was conducted for all modes. The SANR and SMNR angles are given in Table 3.

Table 3.SANR and SMNR angles and for four modes.

Steering angle \Mode	A1	S1	A2	S2
SANR (deg.)	4.8	4.0	2.7	0.9
SMNR (deg.)	5.3	3.7	2.5	0.9

4.1.2 Effect of frequency bandwidth

The frequency bandwidth is a critical factor for guided wave excitation. Assuming a sinusoidal toneburst with center frequency f_c and number of cycles M, the bandwidth is approximated as

$$BW = \frac{2f_c}{M}.$$

The center frequency was kept fixed at 1.9 MHz, thus the bandwidth depends only the number of cycles. As shown in Figure 19, mode A1 is successfully excited using 3 cycles. However, this is not the case for other higher order modes.

To clarify the ideas that follow, mode S3 is studied. Similar results are obtained by studying A3, A2 or S2. The A-scan of mode S3 is shown in Figure 20 (a). Several echoes appear in the signal, with two dominant echoes of approximately equal amplitude. The 2DFFT result is shown in Figure 20 (b). Multiple guided wave modes are observed, and two modes are dominant, namely A3 and S3. Initially, it might seem like each mode depicted in the 2DFFT corresponds to a distinct echo in the A-scan. However, this is not accurate, as clarified by the time-frequency graph presented in Figure 20 (c). According to the time-frequency plot, all echoes span the same frequency range. Therefore, an echo does not correspond to a mode, since each mode is dominant in a distinct frequency range. In fact, each echo that appears in the A-scan is a combination of all modes. The signal corresponds to a bulk-wave bouncing at the top and bottom surfaces of the plate. These types of waves are used in the M-skip method [22].

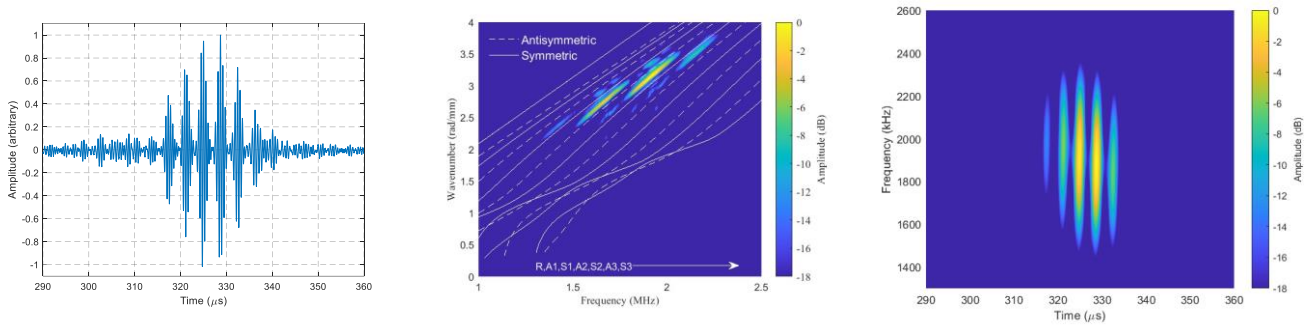

(a) (b) (c)

Figure 20. Mode S3 excited with a 3-cycle toneburst centered at 1.9 MHz: a) A-scan b) 2DFFT c) spectrogram.

As the number of cycles increases, the frequency bandwidth becomes narrower, thus only the targeted mode is excited. The spectrogram of mode S3 at 3, 10 and 15 cycles is shown in Figure 21. The corresponding bandwidths are $1.27, 0.38$ and 0.25 MHz, respectively. As the frequency bandwidth decreases, the excitation becomes single-mode [10].

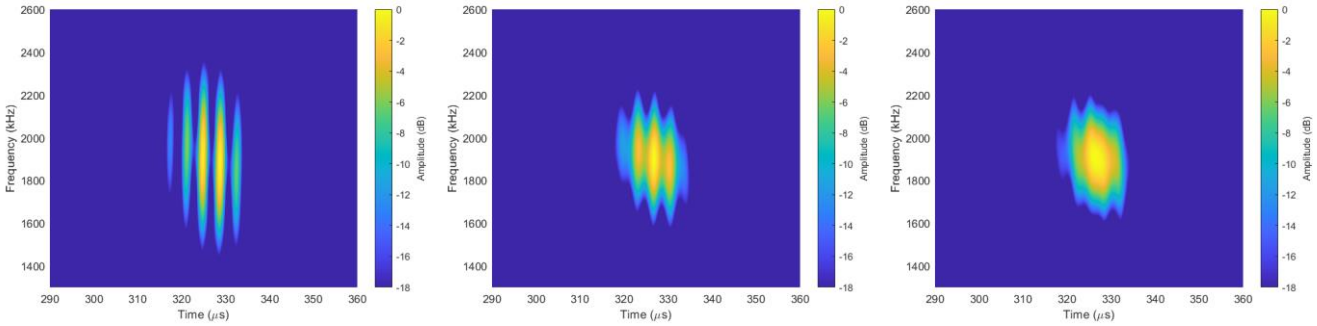

(a) (b) (c)

Figure 21. Spectrogram of mode S3 excited with: (a) 3, (b) 10 and (c) 15 cycles.

4.2 Experimental determination of the through thickness profiles

To determine experimentally the through-thickness profiles of the modes and time of arrival, a first experiment was conducted in pitch-catch configuration. More specifically, a wedge-mounted 32 element, 1

mm pitch array with a nominal frequency of 2.25 MHz emits plane waves, and these are received by a second 128 element 0.75 mm pitch array mounted at the edge of the 10 mm plate. Only the first 13 elements of the latter array are in contact with the sample and so only these are used as receivers. A schematic of the experimental set-up is shown in Figure 22.

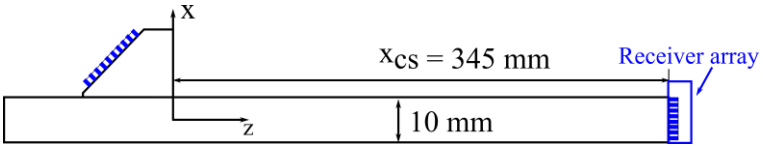

Figure 22. Pitch-catch configuration set-up.

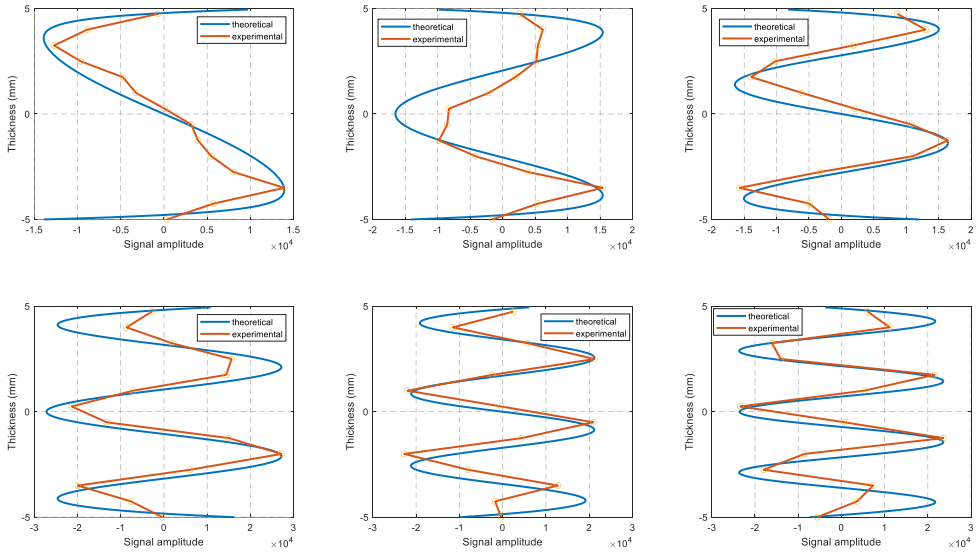

Figure 23. Experimental vs. theoretical through-thickness compressional stress profiles.

Figure 23 presents the experimental vs. theoretical through-thickness profiles. Note that due to a non-viscous couplant layer between the plate and the receiver, the shear components cannot propagate and so these profiles correspond to the σ_{11} profile. As can be seen, there is very good agreement for all modes. This validates the generation of the targeted modes.

The profile $\sigma_{11}(x_{cs}, z, t)$ is obtained experimentally for each mode. Using σ_{11} and the theoretical ratio of σ_{11}/σ_{13}, the σ_{13} profile is obtained. The time of arrival of each mode at the edge is extracted manually. Specifically, the time of arrival is selected at the time where σ_{11} maximizes. The shear and compressional stress profiles are phased by $\pi/4$, thus this phase difference is added to obtain the time of arrival of σ_{13}.

In contrast to simulations, in this case, the edge of the plate was used to extract the amplitude and time of arrival of each mode. To validate the approach, two separate sets of simulations were conducted to generate parameters that are more easily measured experimentally. Specifically, the displacement fields were extracted at the edge of the material. The distance between the edge and the front face of the wedge was 345 mm. The displacement fields were used instead of stress as σ_{11} vanishes at the edge. Then, the displacement fields were extracted at the bulk of the material at the same distance. Direct comparison of the displacement fields showed no phase distortion above 7 degrees was observed in the waveforms for modes A1, S1, A2 and S2. Modes A3 and S3 showed a phase shift of -39 and -90 degrees, respectively. This means that the estimated time of arrival of the first six modes is sufficiently accurate.

4.5 Imaging defects

The experimental set-up for imaging a notch 345 mm away from the front face of the wedge is shown in Figure 24. Data was received and acquired with a phased array controller with 64 transmitter and 64 receiver channels. Data was streamed and stored on a personal computer (PC) for further processing. All experimental

parameters match those in Table 1.

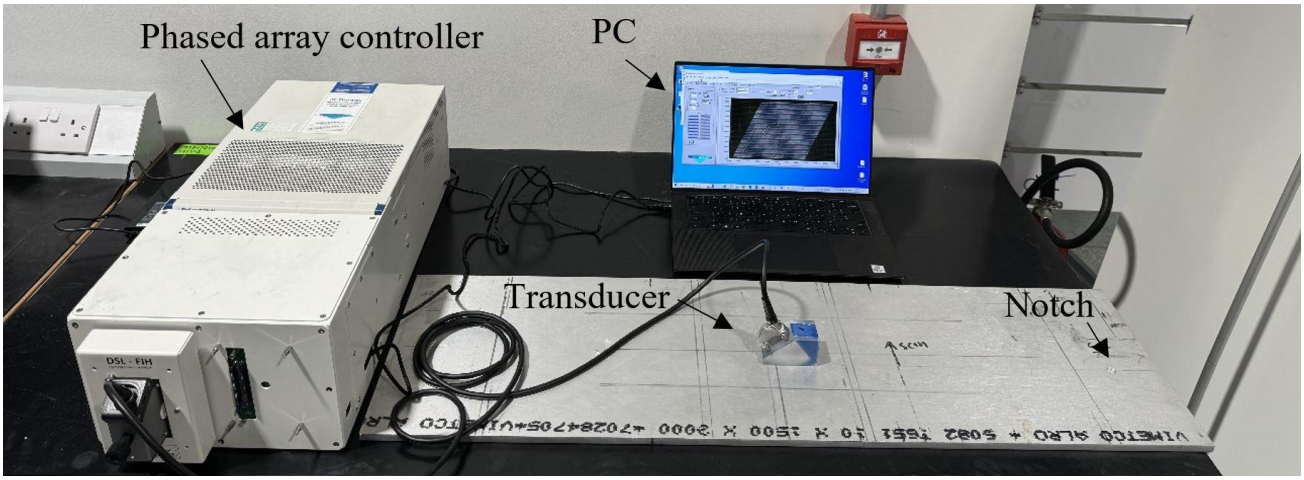

Figure 24. Experimental set-up for imaging a vertical notch.

Figure 25 (a) illustrates the reflection amplitude when focusing at a 55% deep top surface notch. The length of the notch was kept to approximately $5\lambda_{A1}$. The reflection amplitude is close to 0 dB at the face of the notch. Although the amplitude drops away from the notch, a local peak right below the notch is present, thus the depth of the defect is overestimated with 20% error using equation (8). Figure 25 (b) shows the reflection amplitude for a 55% deep bottom surface notch. In this case, the amplitude starts dropping slightly earlier. The defect size is underestimated with an error of 7%. To evaluate the effect of adding two higher order modes to the technique, modes $A3$ and $S3$ were added to the sum of equation (2). The result is shown in Figure 25 (c) and (d). The results are very similar to those in Figure 25. This validates experimentally that no significant contribution is gained by adding modes A3 and S3. The depth estimation error is slightly higher compared to the simulation results. This is possibly due to small error in the time of arrival estimation of the modes. Overall, the experimental results are in good agreement with simulations.

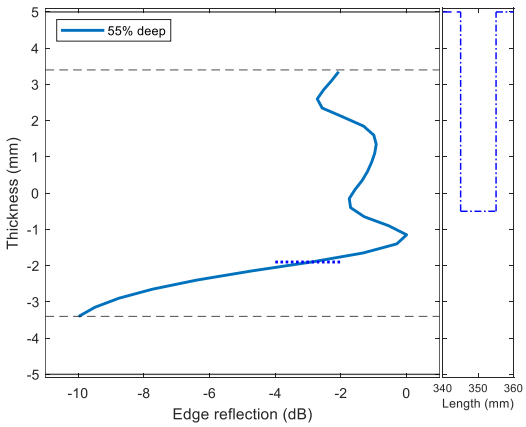

(a)

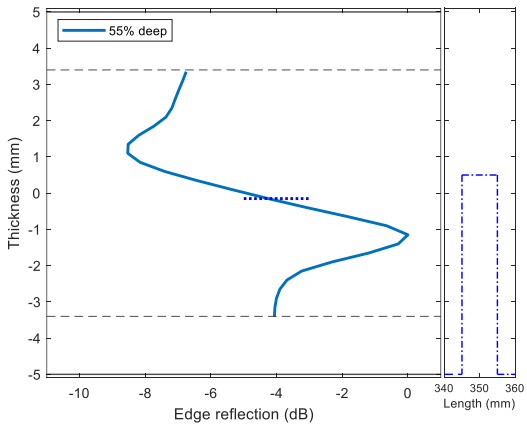

(b)

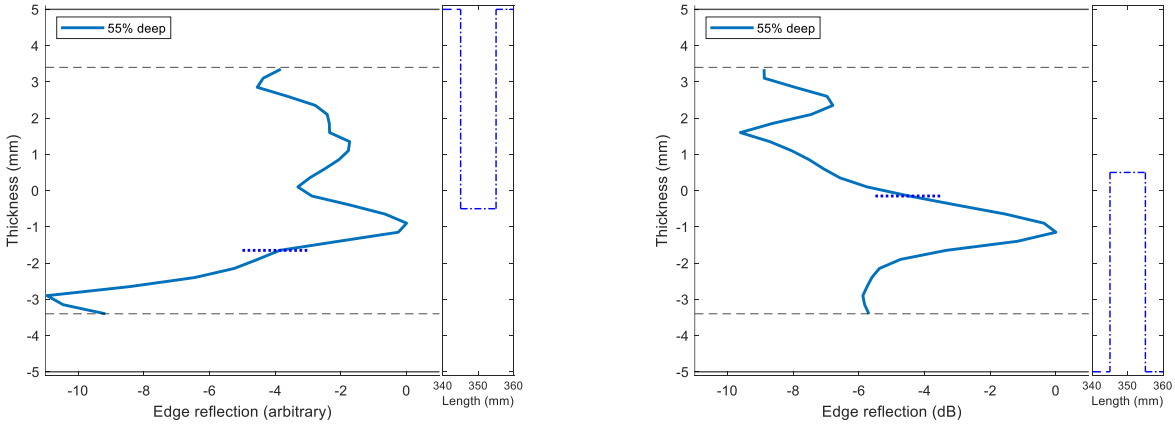

(c) (d)

Figure 25. Experimental results from through-thickness focusing at a 5.5 mm deep 10 mm diameter (a) top surface notch using 4 modes, (b) bottom surface notch using 4 modes, (c) top surface notch using 6 modes and (d) bottom surface notch using 6 modes.

Compared to simulation results, the error in depth estimation exhibits a slight increase, which can be attributed to various contributing factors. Firstly, small variations in the thickness of the plate may introduce small errors in the estimation of the time of arrival for each mode. Additionally, in contrast to simulations, the time of arrival was determined using the edge of the plate. This introduces small phase shifts in each mode that can affect focusing. Furthermore, positioning discrepancies in the probe between the pitch-catch (see Figure 22) and pulse echo (see Figure 24) experiments might contribute to issues in focusing. Also, errors can be introduced in the calculation of the weight functions. The weights are calculated using the analytical through-thickness profiles. Although these agree well with the experimental ones (see Figure 23), small differences might lead to errors in the derivation of the weight functions. While these error sources may be individually small, their cumulative impact may either mitigate or amplify the overall error in depth estimation.

5. Conclusion

In this work, a focusing technique using guided waves was developed to image the volume of plate-like structures at locations up to 2-3 m away from the probe. First, emphasis was placed on single-mode guided wave excitation at high frequency-thickness products. Specifically, it was shown that multiple modes can be solely excited using an array probe, provided that both the excitation and frequency spectrums are narrowband. Then, guided wave modes were superimposed to focus on a single point at a specified distance from the transducer and at a desired depth. By weighting the modes, the focal point was swept across the thickness of the plate. It was found that the first four higher order modes yield good focusing results, and adding more modes does not significantly improve the focusing resolution. Analytical computations showed that the focusing ability decreases as the focal point approaches the top or bottom surfaces of the plate. Effectively, a 1.5 mm ‘dead zone’ starts from both the top and bottom surfaces. Inside this region, focusing is not possible. Additionally, thickness variations did not affect focusing, as long as they did not extend significantly, i.e., less than 9 wavelengths for a 1 mm wall loss anomaly. Next, simulations were performed. A variety of notches with varying lengths and depths were modelled. Their depth was accurately estimated, provided it was larger than the focal width. Notch length did not affect depth estimation, even for lengths shorter than the wavelength. Finally, experiments were conducted using two 55% deep notches, one on the top surface and the other on the bottom surface. As expected, a high reflection amplitude was obtained when focusing on the face of the notch, whereas focusing on the intact region of the sample led to a drop in amplitude. The error was slightly higher compared to simulation results, but the overall performance was in good agreement with theoretical and numerical results. Future work includes further simulation and experimental validation of the technique. A detailed study on the effect of defect width is required, employing full 3D simulations and the manufacture of more defects. The technique can be extended to different guided waves, such as shear horizontal modes.

Acknowledgments: This research was funded by the Advanced Nuclear Research Centre (ANRC) grant number EP/R004889/1.

References

[1] G. Dobie, S. Gareth Pierce, G. Hayward, The feasibility of synthetic aperture guided wave imaging to a mobile sensor platform, NDT E Int. 58 (2013) 10–17. https://doi.org/10.1016/j.ndteint.2013.04.002.
[2] D.N. Alleyne, P. Cawley, Optimization of lamb wave inspection techniques, NDT E Int. 25 (1992) 11–22. https://doi.org/10.1016/0963-8695(92)90003-Y.
[3] O. Trushkevych, M. Tabatabaeipour, S. Dixon, M.D.G. Potter, G. Dobie, C. Macleod, R.S. Edwards, Miniaturised SH EMATs for Fast Robotic Screening of Wall Thinning in Steel Plates, IEEE Sens. J. 21 (2021) 1386–1394. https://doi.org/10.1109/JSEN.2020.3021526.
[4] P. Belanger, High order shear horizontal modes for minimum remnant thickness, Ultrasonics. 54 (2014) 1078–1087. https://doi.org/10.1016/j.ultras.2013.12.013.
[5] S. Fletcher, M.J.S. Lowe, M. Ratassepp, C. Brett, Detection of axial cracks in pipes using focused guided waves, J. Nondestruct. Eval. 31 (2012) 56–64. https://doi.org/10.1007/s10921-011-0120-x.
[6] R. Content, Utilization of guided elastic waves for the characterization of circumferential cracks in hollow cylinders, 3775 (2015) 3769–3775.
[7] M.J.S. Lowe, D.N. Alleyne, P. Cawley, Defect detection in pipes using guided waves, 1998.
[8] A. Demma, P. Cawley, M. Lowe, A.G. Roosenbrand, B. Pavlakovic, The reflection of guided waves from notches in pipes: A guide for interpreting corrosion measurements, NDT E Int. 37 (2004) 167–180. https://doi.org/10.1016/j.ndteint.2003.09.004.
[9] C. Jayaraman, C. V. Krishnamurthy, K. Balasubramaniam, Higher order modes cluster (HOMC) guided waves - A new technique for ndt inspection, in: AIP Conf. Proc., American Institute of Physics, 2009: pp. 121–128. https://doi.org/10.1063/1.3114094.
[10] K. Tzaferis, M. Tabatabaeipour, G. Dobie, D. Lines, C.N. MacLeod, Single-mode Lamb wave excitation at high-frequency-thickness products using a conventional linear array transducer, Ultrasonics. (2022) 106917. https://doi.org/10.1016/j.ultras.2022.106917.
[11] K. Shivaraj, K. Balasubramaniam, C. V. Krishnamurthy, R. Wadhwan, Ultrasonic circumferential guided wave for pitting-type corrosion imaging at inaccessible pipe-support locations, J. Press. Vessel Technol. Trans. ASME. 130 (2008) 0215021–12150211. https://doi.org/10.1115/1.2892031.
[12] J. Chandrasekaran, I. Anto, K. Balasubramaniam, K.S. Venkataraman, Higher order modes cluster (HOMC) guided waves for online defect detection in annular plate region of above-ground storage tanks, Insight Non-Destructive Test. Cond. Monit. 51 (2009) 606–611. https://doi.org/10.1784/insi.2009.51.11.606.
[13] P. Khalili, P. Cawley, The choice of ultrasonic inspection method for the detection of corrosion at inaccessible locations, NDT E Int. 99 (2018) 80–92. https://doi.org/10.1016/j.ndteint.2018.06.003.
[14] D. Cirtautas, V. Samaitis, L. Mažeika, R. Raišutis, E. Žukauskas, Selection of Higher Order Lamb Wave Mode for Assessment of Pipeline Corrosion, Metals (Basel). 12 (2022). https://doi.org/10.3390/met12030503.
[15] P. Khalili, P. Cawley, Excitation of Single-Mode Lamb Waves at High-Frequency-Thickness Products, IEEE Trans. Ultrason. Ferroelectr. Freq. Control. 63 (2016) 303–312. https://doi.org/10.1109/TUFFC.2015.2507443.
[16] G. Veit, P. Bélanger, An ultrasonic guided wave excitation method at constant phase velocity using ultrasonic phased array probes, Ultrasonics. 102 (2020). https://doi.org/10.1016/j.ultras.2019.106039.
[17] J. L.Rose, Joseph L.Rose - Ultrasonic Waves in solid media, Cambridge University Press, 2008.
[18] O.C. Zienkiewicz, R.L. Taylor, D.D. Fox, The Finite Element Method for Solid and Structural Mechanics, 7th ed., Elsevier Ltd., 2014.
[19] Onscale software, (n.d.). https://onscale.com/ (accessed May 18, 2023).
[20] M. Drozdz, L. Moreau, M. Castaings, M.J.S. Lowe, P. Cawley, Efficient numerical modelling of absorbing regions for boundaries of guided waves problems, in: AIP Conf. Proc., 2006: pp. 126–133. https://doi.org/10.1063/1.2184520.
[21] R.D. Cook, D.S. Malkus, M.E. Plesha, R.J. Witt, Concepts and Applications of Finite Element Analysis, 4th Edition, 4th ed., Wiley, 2001.
[22] S.F. Burch, N.J. Collett, S. Terpstra, M. V. Hoekstra, M-skip: A quantitative technique for the

measurement of wall loss in inaccessible components, Insight Non-Destructive Test. Cond. Monit. 49 (2007) 190–194. https://doi.org/10.1784/insi.2007.49.4.190.